

Mesoporous Spherical Aggregates of Anatase Nanocrystals with Wormhole-like Framework Structures: Their Chemical Fabrication, Characterization, and Photocatalytic Performance

Hui Wang,^{†,‡} Jian-Jun Miao,[‡] Jian-Min Zhu,[§] Hong-Min Ma,[‡] Jun-Jie Zhu,^{*,‡} and Hong-Yuan Chen[‡]

Key Lab of Analytical Chemistry for Life Science, Department of Chemistry, Nanjing University, Nanjing 210093, China and National Laboratory of Solid State of Microstructures, Nanjing University, Nanjing 210093, China

Received September 3, 2004

A facile and efficient approach for the fabrication of mesoporous spherical aggregates of anatase nanocrystals is reported in this paper. Cetyltrimethylammonium bromide was used as the structure-directing agent, and the interaction between cyclohexane microdroplets and the cetyltrimethylammonium bromide self-assemblies led to the assembly of 4–5-nm-sized anatase nanocrystals into spherical aggregates with mesoporous structures. The as-prepared anatase powders exhibited high photocatalytic activity and could be effectively used as the catalyst for the room-temperature photodegradation of a variety of organic dye pollutants in aqueous media including methyl orange, bromopyrogallol red, and methylene blue.

I. Introduction

Assembly of nanometer-sized building blocks into desired mesoscopic structures has stimulated increasing attention in recent years.^{1,2} The development of new and efficient approaches for the combination of nanocrystals into ordered structures not only provides us with a better understanding of the factors governing the formation of the nanocrystal assembly motifs, but also opens new opportunities for the fabrication of nanodevices with controllable and optimized functions. Self-assembly based on selective control of noncovalent interactions provides a powerful tool for the creation of structured systems with mesoscopic dimensions. Amphiphile molecules can form a large variety of three-dimensional supramolecular structures through noncovalent interactions, which can be used to direct the multiscale ordering of nanocrystals into desired mesostructures.

The past decade has seen rapid advances in the fabrication of mesoporous solid-state materials. Since the discovery of mesoporous aluminosilicate materials (M41S) with uniformly sized pores,³ a variety of ordered mesoporous silica-based materials have been synthesized by using the supramolecular assembly of amphiphile molecules as a template. The supramolecular templating

approach has also been extended to the synthesis of mesoporous non-siliceous oxides. Transition-metal oxides have some advantages over aluminosilicate materials for use in electromagnetics, photoelectronics, and catalysis because transition-metal atoms can exist in various oxidation states. However, synthesis and structures of transition-metal oxides can be much more complicated than oxides of main group metals because of the multitude of different coordination numbers and oxidation states. Up to now, a series of mesoporous transition-metal oxides, such as oxides of tungsten,⁴ vanadium,⁵ zinc,⁶ niobium,⁷ zirconium,^{8,4c} tantalum,^{9,4c} hafnium,^{10,4c} and manganese,¹¹ have been synthesized via various supramolecular templating routes. The obtained mesoporous oxides discussed above usually consist of amorphous walls and thus can be viewed as glasses with ordered pores. Since many applications require crystalline materials with specific crystalline structures, it would be advantageous to synthesize mesoporous materials with desired crystalline frameworks.¹²

Semiconducting transition-metal oxides participate in a variety of photocatalytic reactions. Titania is one of the most intensively studied semiconductors for the photocatalysis.¹³ It can be used in the treatment of environ-

* To whom correspondence should be addressed. E-mail: jjzhu@nju.edu.cn; fax: +86-25-83317761.

[†] H. Wang is currently a Ph.D. student in Department of Chemistry at Rice University, Houston, Texas.

[‡] Key Lab of Analytical Chemistry for Life Science.

[§] National Laboratory of Solid State of Microstructures.

(1) For some recent reviews, see (a) Hamley, I. W. *Nanotechnology* **2003**, *14*, R39. (b) Bowden, N. B.; Weck, M.; Choi, I. S.; Whitesides, G. M. *Acc. Chem. Res.* **2001**, *34*, 231. (c) Kimizuka, N. *Curr. Opin. Chem. Biol.* **2003**, *7*, 702. (d) Balazs, A. C. *Curr. Opin. Solid State Mater. Sci.* **2003**, *7*, 27. (e) Palmqvist, A. E. C. *Curr. Opin. Colloid Interface Sci.* **2003**, *8*, 145. (f) Colfen, H.; Mann, S. *Angew. Chem., Int. Ed.* **2003**, *42*, 2350.

(2) Davis, S. A.; Breulmann, M.; Rhodes, K. H.; Zhang, B.; Mann, S. *Chem. Mater.* **2001**, *13*, 3218.

(3) (a) Kresge, C. T.; Leonowicz, M. E.; Roth, W. J.; Vartuli, J. C.; Beck, J. S. *Nature* **1992**, *359*, 710. (b) Beck, J. S.; Vartuli, J. C.; Roth, W. J.; Leonowicz, M. E.; Kresge, C. T.; Schmitt, K. D.; Chu, C. T.-W.; Olson, D. H.; Sheppard, E. W.; McCullen, S. B.; Higgins, J. B.; Schlenker, J. L. *J. Am. Chem. Soc.* **1992**, *114*, 10834.

(4) (a) Huo, Q.; Margolese, D. I.; Ciesla, U.; Feng, P.; Gier, T. E.; Sieger, P.; Leon, R.; Petroff, P. M.; Schuth, F.; Stucky, G. D. *Nature* **1994**, *368*, 317. (b) Huo, Q.; Margolese, D. I.; Ciesla, U.; Demuth, D. G.; Feng, P.; Gier, T. E.; Sieger, P.; Firouzi, A.; Chmelka, B. F.; Schuth, F.; Stucky, G. D. *Chem. Mater.* **1994**, *6*, 1176. (c) Yang, P. D.; Zhao, D. Y.; Stucky, G. D. I. Chmelka, B. F.; Stucky, G. D. *Nature* **1998**, *396*, 152.

(5) (a) Abe, T.; Taguchi, A.; Iwamoto, M. *Chem. Mater.* **1995**, *7*, 1429. (b) Luca, V.; MacLachlan, D. J.; Hook, J. M.; Withers, R. *Chem. Mater.* **1995**, *7*, 2220.

(6) Zhao, D.; Goldfarb, D. *Chem. Mater.* **1996**, *8*, 2571.

(7) Antonelli, D. M.; Ying, J. Y. *Angew. Chem., Int. Ed. Engl.* **1996**, *35*, 426.

(8) (a) Ciesla, U.; Schacht, S.; Stucky, G. D.; Unger, K. K.; Schuth, F. *Angew. Chem., Int. Ed. Engl.* **1996**, *35*, 541. (b) Kim, A.; Bruinsma, P.; Chen, Y.; Wang, L. Q.; Liu, J. *Chem. Commun.* **1997**, 161. (c) Pacheco, G.; Zhao, E.; Garcia, A.; Sklyarov, A.; Fripiat, J. J. *Chem. Commun.* **1997**, 491.

(9) Antonelli, D. M.; Ying, J. Y. *Chem. Mater.* **1996**, *8*, 874.

(10) Tian, Z.-R.; Tong, W.; Wang, J.-Y.; Duan, N.-G.; Krishnan, V. V.; Suib, S. L. *Science* **1997**, *276*, 926.

(11) Liu, P.; Liu, J.; Sayari, A. *Chem. Commun.* **1997**, 577.

mental pollutants, for example, the photoassisted degradation of organic chloride compounds, phenol derivatives, azo-dye molecules, and organic phosphorus peptides, and so forth. Environmental purification using TiO_2 photocatalysts has attracted a great deal of attention with the increasing number of recent environmental problems in the world. Titania, especially in its anatase phase, can also find wide applications in dye-sensitized solar cells.^{13f,14} The synthesis of mesoporous titania with crystalline frameworks is of particular interest because the success in many of these applications relies on crystalline titania with ordered nanodimensional porous structures. In 1995, mesoporous titania was first synthesized by using alkyl phosphate surfactants as the template and titanium isopropoxide bisacetylacetonate as the precursor.¹⁵ However, phosphorus species from the template was bounded so strongly to the molecular sieve that its possible applications as a catalyst or catalyst support were limited. Phosphorus-free mesoporous titania could be synthesized by using an amine surfactant in combination with a dry aging technique.¹⁶ Yang et al.^{4c} also reported the synthesis of thermally stable and large-pore mesoporous titania by using block copolymers as structure-directing agents. Using cationic surfactant cetyltrimethylammonium chloride ($\text{C}_{16}\text{TMA}^+\text{Cl}^-$) as a structure-directing agent, and soluble peroxytitanate as a precursor, Do Trong On¹⁷ synthesized hexagonal and lamellar titanium oxide mesostructures hydrothermally in the presence of sodium cations and tetramethylammonium hydroxide, respectively. Pang and co-workers¹⁸ prepared highly ordered lamellar titania mesophase by hydrothermal treatment of aqueous solutions containing cetyltrimethylammonium bromide (CTAB), tetramethylammonium hydroxide (TMAOH), and tetrabutylorthotitanate (TBOT). Khushalani et al.¹⁹ used cetyltrimethylammonium glycotitanate as the precursor to synthesize partially ordered mesoporous titania in nonaqueous solvents. Gedanken and co-workers²⁰ established a sonochemical method for the fabrication of mesoporous titania by using long-chain neutral amines as the structure-directing agent. The as-prepared mesoporous titania presents a wormhole-like framework structure, which is different from the long-range hexagonal or lamellar mesostructures. However, in all the cases mentioned above, the obtained mesoporous titania has amorphous wall frameworks. The synthesis of mesoporous titania with crystalline frameworks still remains a great challenge. Only very recently has the

first example of well-defined mesoporous titania with crystalline framework structures been reported.²¹ By using a novel room-temperature ionic liquid solvent, 1-butyl-3-methylimidazolium-tetrafluoroborate, 2–3-nm-sized titania nanocrystals were successfully synthesized and these nanocrystals could self-assemble into mesoporous spherical aggregates simultaneously in this ionic liquid solvent.

In this paper, we report a facile and efficient approach for the fabrication of mesoporous spherical aggregates of anatase nanocrystals. This approach is based on the controlled hydrolysis of titanium(IV) sulfate in acidic aqueous media. A cationic surfactant, cetyltrimethylammonium bromide (CTAB), was used as the structure-directing agent, and the interaction between cyclohexane microdroplets and the CTAB self-assemblies leads to the assembly of anatase nanocrystals into spherical aggregates with wormhole-like mesoporous structures. This wormhole channel motif is a potentially important structural feature for catalytic activity, in part, because channel branching within the framework can facilitate access to reactive sites on the framework wall. To study the morphology, structure, and properties of the product, a variety of techniques were employed, including powder X-ray diffraction, transmission electron microscopy, nitrogen adsorption–desorption, Fourier transform infrared spectroscopy, X-ray electron spectroscopy, diffuse reflection spectroscopy, and photoluminescent spectroscopy. The as-prepared mesoporous aggregates of anatase nanocrystals have been used to catalyze the photoinduced degradation of various types of organic dye molecules which are representative environmental pollutants in wastewater, such as methyl orange (azoic dye), bromopyrogallol red (phenol derivative), and methylene blue (heteropolyaromatic dye).

II. Experimental Section

Chemicals. All the reagents used in our experiments were of analytical purity and were used without further purification. Titanium(IV) sulfate ($\text{Ti}(\text{SO}_4)_2$), 98% sulfuric acid, and cetyltrimethylammonium bromide ($\text{C}_{19}\text{H}_{42}\text{BrN}$, CTAB) were purchased from Shanghai Chemical Reagents Corporation (Shanghai, China). Cyclohexane, 200-proof ethanol and acetone were purchased from Nanjing Chemical Reagents Factory (Nanjing, China). The organic dyes including methyl orange, bromopyrogallol red, and methylene blue were all purchased from Shanghai Chemical Reagents Corporation.

Synthesis. In a typical procedure, 2.0 g of CTAB was dissolved in 100 mL distilled water in a 200 mL round-bottom flask. Then 2.0 mL 98% sulfuric acid, 2.5 mL cyclohexane, and 1.0 g $\text{Ti}(\text{SO}_4)_2$ were introduced into the CTAB solution in sequence. After stirring for 1 h, a transparent microemulsion formed. A condensing tube was connected to the flask and the reactant mixture was kept refluxing at around 100 °C for 1 h. When the reaction was finished, a white precipitate appeared. After cooling to room temperature, the precipitate was centrifuged at a rotation rate of 12000 rounds/s, washed with distilled water, ethanol, and acetone repeatedly, and dried in air at room temperature. The final product was in the form of snow-white powders and was collected for characterization.

Characterization. Both small-angle X-ray powder diffraction (SAXRD) and wide-angle X-ray powder diffraction measurements were performed on a Philips X-ray diffractometer X'Pert Pro MPD with graphite-monochromatized $\text{Cu K}\alpha$ radiation ($\lambda = 1.5418 \text{ \AA}$). The acceleration voltage was 35.0 kV with a 150.0 mA current flux. XRD patterns were taken of the powders attached to a glass slide, and data were collected with a scanning rate of 4°/min and a sample interval of 0.02°. Transmission electron micrograph (TEM) and selected area electron diffraction (SAED)

(12) (a) Liu, J.; Kim, A.; Wang, L. Q.; Palmer, B. J.; Chen, Y. L.; Bruinsma, P.; Bunker, B. C.; Exarhos, G. J.; Graff, G. L.; Rieke, P. C.; Fryxell, G. E.; Virden, J. W.; Tarasevich, B. J.; Chick, L. A. *Adv. Colloid Interface Sci.* **1996**, *69*, 131. (b) Raman, N. K.; Anderson, M. T.; Brinker, C. J. *Chem. Mater.* **1996**, *8*, 1682. (c) Qi, L.; Ma, J.; Cheng, H.; Zhao, Z. *Langmuir* **1998**, *14*, 2579.

(13) (a) Hoffmann, M. R.; Martin, S. T.; Choi, W. Y.; Bahnemann, D. W. *Chem. Rev.* **1995**, *95*, 69. (b) Rajeshwar, K. *J. Appl. Electrochem.* **1995**, *25*, 1067. (c) Dillert, R.; Cassano, A. E.; Goslich, R.; Bahnemann, D. *Catal. Today* **1999**, *54*, 267. (d) Linsebrügler, A. L.; Lu, G.; Yates, J. T. *Chem. Rev.* **1995**, *95*, 735. (e) Fox, M. A.; Dulay, M. T. *Chem. Rev.* **1993**, *93*, 341. (f) Hagfeldt, A.; Gratzel, M. *Chem. Rev.* **1995**, *95*, 49.

(14) (a) O'Regan, B.; Gratzel, M. *Nature* **1991**, *352*, 737. (b) Nazeeruddin, M. K.; Kay, A.; Rodicio, L.; Humphry-Baker, R.; Muler, E.; Liska, P.; Vlachopoulos, N.; Gratzel, M. *J. Am. Chem. Soc.* **1993**, *115*, 6382.

(15) Antonelli, D. M.; Ying, Y. J. *Angew. Chem., Int. Ed. Engl.* **1995**, *34*, 2014.

(16) Antonelli, D. M. *Microporous Mesoporous Mater.* **1999**, *30*, 315.

(17) On, D. T. *Langmuir* **1999**, *15*, 8561.

(18) Lin, W.; Pang, W.; Sun, J.; Shen, J. *J. Mater. Chem.* **1999**, *9*, 641.

(19) Khushalani, D.; Ozin, G. A.; Kuperman, A. *J. Mater. Chem.* **1999**, *9*, 1491.

(20) (a) Wang, Y.; Tang, X.; Yin, L.; Huang, W.; Hacheco, Y. R.; Gedanken, A. *Adv. Mater.* **2000**, *12*, 1183. (b) Wang, Y.; Chen, S.-G.; Tang, X.-H.; Palchik, O.; Zaban, A.; Gedanken, A. *J. Mater. Chem.* **2001**, *11*, 521.

(21) Zhou, Y.; Antonietti, M. *J. Am. Chem. Soc.* **2003**, *125*, 14960.

patterns were recorded on a JEOL-JEM 200CX transmission electron microscope, using an accelerating voltage of 200 kV. High-resolution transmission electron micrographs (HRTEM) were obtained by employing a JEOL-4000EX high-resolution transmission electron microscope with a 400 kV accelerating voltage. A conventional CCD video camera was employed to digitize the micrographs, which were then processed using Digital Micrograph software. The samples used for TEM and HRTEM observations were prepared by dispersing some products in ethanol followed by ultrasonic vibration for 15 min and then placing a drop of the dispersion onto a copper grid coated with a layer of amorphous carbon. N_2 adsorption-desorption isotherms were collected on a Micromeritics-Gemini adsorption analyzer at 77 K after the sample had been dried at 170 °C for 1 h. The BET surface area was calculated from the linear part of the BET plot. The pore diameter is calculated by $4 \times \text{pore volume/surface area}$. The pore size distribution plots are obtained by using the Barret-Joyner-Halenda (BJH) model. Thermogravimetric analysis (TGA) was conducted on an LCT-1 type thermoanalyzer in air. IR spectroscopy was carried out on a Bruker IFS66 Fourier transform infrared (FT-IR) spectrometer (Bruker Co.) in the single-beam mode over the range of 500–4000 cm^{-1} at room temperature. The sample powders were milled in KBr wafer. X-ray photoelectron spectra (XPS) were recorded on an ESCALAB MK II X-ray photoelectron spectrometer, using nonmonochromatized $\text{Mg K}\alpha$ X-ray as the excitation source, and choosing C 1s (284.6 eV) as the reference line. Diffuse reflection spectra (DRS) were recorded on a Shimadzu UV-2100 recording spectrophotometer scanning from 700 to 200 nm at room temperature. The scanning rate was 500 nm/min, and BaSO_4 was used as a reference. The photoluminescence measurements were carried out by using a Shimadzu RF PC-5301 spectrofluorophotometer at room temperature. A 150 W xenon lamp were used as the excitation source. The samples for photoluminescence measurements were colloidal aqueous solutions containing 0.1 mg/mL TiO_2 .

Investigations of Photocatalytic Properties. The photocatalytic degradation of various organic dyes including methyl orange, bromopyrogallol red, and methylene blue was investigated by using the as-prepared mesoporous anatase spherical aggregates as the catalyst. The ultraviolet irradiation source is a 500 W, column-like, high-pressure mercury lamp with a main emission at λ of 290 nm. The lamp was placed inside a cylindrical circulating water quartz jacket and water was circulated through the annulus to avoid overheating of the lamp during the reaction. Different loadings of the as-prepared anatase powders were dispersed in the dye aqueous solutions. Then, the mixture solutions were placed in a glass beaker about 10 cm away from the center of the lamp and exposed to ultraviolet irradiation at room temperature. Samples were taken periodically from the reaction mixture by using a pipet and were analyzed by UV-visible absorption spectroscopy after filtration. The UV-visible absorption spectroscopic measurements were performed on a Shimadzu UV-2100 recording spectrophotometer.

III. Results and Discussions

Structural and Compositional Analysis. The SAXRD pattern of the final product is shown in Figure 1. An intense peak is observed with a d -spacing corresponding to ca. 4.5 nm. This d -spacing value represents an average distance between the inorganic walls, which can be calculated from the Bragg's law. XRD peaks at high d -spacing generally correspond to an ordered supramolecular templated inorganic structure.²² This peak appears to be broadening with a broad tail that extends to approximately $2\theta = 6^\circ$ and there are no higher order peaks clearly distinguished, which indicates a short-range-ordered framework pore structure.^{17,19,20} The wide-angle XRD pattern of this sample is shown in the inset of Figure 1. All the diffraction peaks in the 2θ range of 20 – 70° can be indexed to be a pure anatase phase for TiO_2 with a

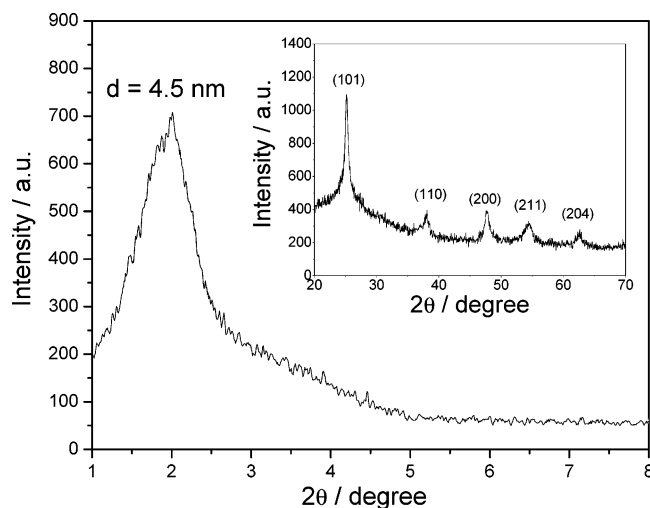


Figure 1. SAXRD pattern of the as-prepared anatase powder and wide-angle XRD pattern of the as-prepared anatase powder (inset).

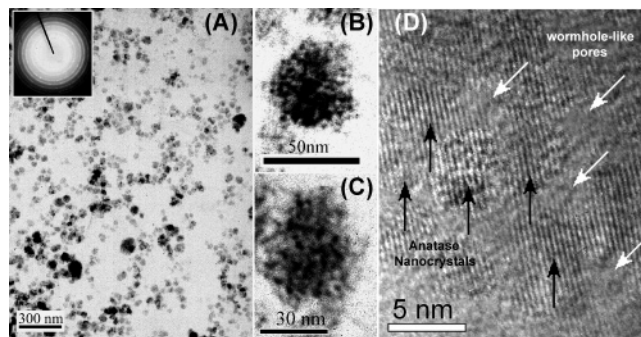


Figure 2. (A) Typical TEM image of the as-prepared anatase powders, revealing the overall dimensions and morphologies of the sample. The inset is a SAED pattern. (B) and (C) TEM images of individual mesoporous spherical aggregates with higher magnifications. (D) HRTEM image showing the microstructures inside an individual mesoporous aggregate.

body centered tetragonal crystalline structure.²³ The cell parameters are calculated to be $a = b = 3.793 \text{ \AA}$ and $c = 9.570 \text{ \AA}$, which are in good agreement with the literature values.²³ No peaks of any other phases of titania such as rutile and brookite are detected. The peaks are apparently broadening, indicating that the sample is composed of small-sized nanocrystalline particles. According to the Debye-Scherrer formula,²⁴ an average size of the crystallites of about 5 nm is derived from the half-height breadth of the five peaks.

The morphology, dimensions, and structures are characterized by TEM and HRTEM measurements. Figure 2A is a representative TEM image with relatively low magnification that reveals the overall morphology of the product. It is apparent that this sample is composed of spheres with diameters of 30–50 nm. Structural information of these spheres is obtained from the SAED analysis. A typical SAED pattern recorded on an individual sphere with a convergent electron beam is shown in the inset of Figure 2A. It shows a set of rings that correspond to the anatase phase, indicating the polycrystalline nature of these spheres. This was further verified by TEM images of individual spheres with higher magnifications, which

(23) Joint Committee on Powder Diffraction Standards (JCPDS), No. 71-1168; International Center for Diffraction Data: Newton Square, PA, 1999.

(24) Klug, H.; Alexander, L. In *X-ray Diffraction Procedures*; Wiley: New York, 1962; p 125.

(22) Tanev, P. T.; Pinnavaia, T. J. *Science* **1995**, *267*, 865.

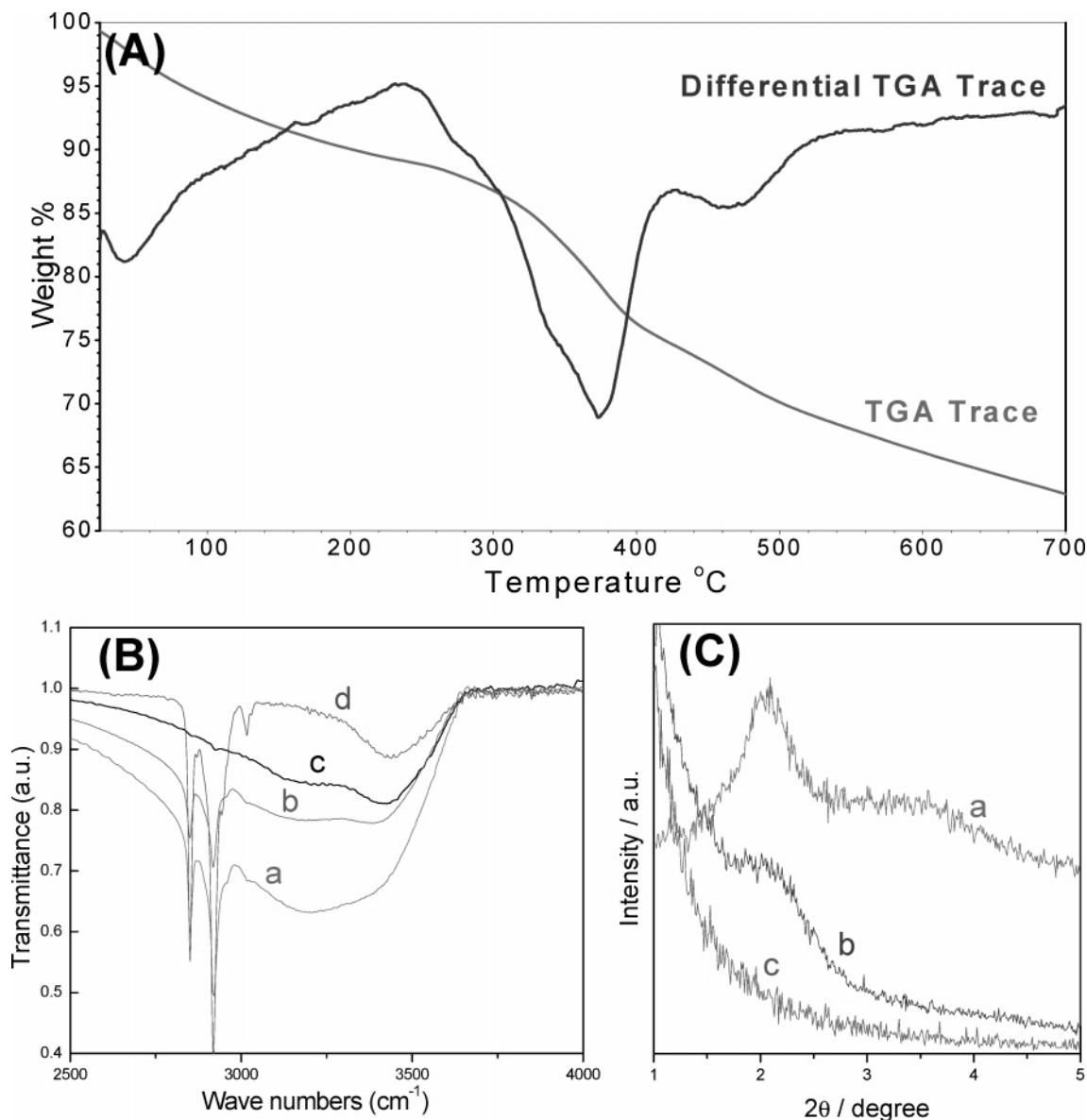


Figure 3. (A) TGA trace and differential TGA trace of the as-prepared mesoporous aggregate of anatase nanocrystals. (B) FT-IR spectra of (a) the as-prepared mesoporous aggregate of anatase nanocrystals, (b) after calcinations at 150 °C for 2 h, (c) after calcinations at 400 °C for 2 h, and (d) commercial CTAB. (C) SAXRD patterns of the as-prepared anatase powders after calcinations at (a) 100 °C, (b) 200 °C, and (c) 400 °C for 2 h.

are shown in Figure 2B and 2C. As can be clearly observed, each sphere is a spherical aggregate of hundreds of individual small spherical nanoparticles. The diameters of these nanoparticles are in the range of 4–5 nm, which is in agreement with the average size estimated from the XRD pattern. These nanoparticles are linked one by one to form a wormhole-like porous structure. Further information about the microstructures of the as-prepared anatase mesophase is provided by HRTEM investigations. As shown in Figure 2D, within an individual aggregate, the pore openings (indicated by the white arrows) are surrounded by several nanocrystals (indicated by the black arrows). Each individual nanocrystal depicts the well-resolved crystalline planes with d -spacing of 3.5 Å. This spacing typically corresponds to the [101] planes of anatase. These nanocrystals connect with one another to form crystalline framework walls of the mesoporous system. The observed average pore diameter is about 3 nm. The pore-to-pore distance is around 5 nm, which is roughly in accordance with that estimated according to the SAXRD pattern.

Figure 3A displays the TGA weight loss and the corresponding derivative curve of the as-prepared mesoporous anatase powder. The TGA curve shows two distinct weight losses arising from the desorption of water adsorbed on the surface of the sample (from room temperature to 200 °C) and the decomposition of the organic template, the CTAB molecules incorporated in the inorganic framework (from 280 to 600 °C). The total amount of the CTAB present in the sample was about 25 wt %. It indicates that there is a certain amount of surfactant molecules (CTAB) attached to the inorganic framework, and it is difficult to remove these surfactants just by the washing process. It is believed that the remaining surfactant molecules form a thin layer between the nanocrystals that acts as a binder to hold the nanocrystals together and thus keep the mesoporous structures. The derivative curve presents a broad peak centered at 370 °C and a small shoulder at 470 °C during the second weight loss. The peak at 370 °C may be attributed to the decomposition of CTAB around the opening and shallow part of the pores, while the shoulder peak at 470 °C may be attributed to the

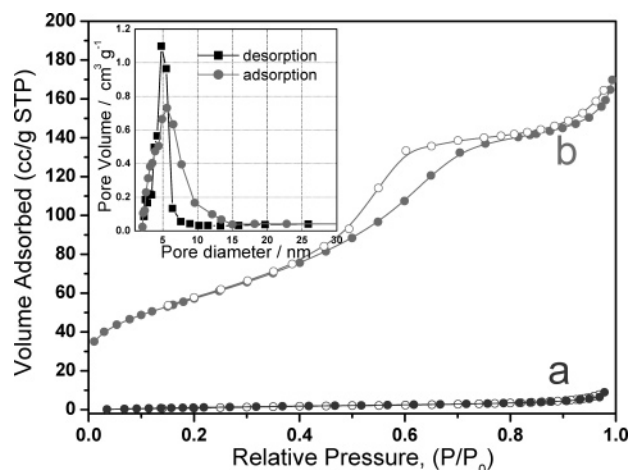


Figure 4. N_2 adsorption–desorption isotherm of (a) the as-prepared mesoporous anatase and (b) the sample after calcination at $400\text{ }^\circ\text{C}$ for 2 h. The inset is the adsorption and desorption pore-size distribution of the sample calcined at $400\text{ }^\circ\text{C}$.

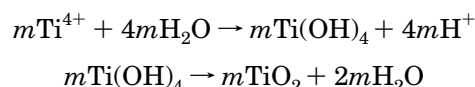
decomposition of those CTAB molecules trapped deep inside the pore channels. The presence of CTAB molecules in the as-prepared mesoporous anatase was further verified by FT-IR spectroscopic measurements. As shown in Figure 3B, two typical absorption peaks at 2918 and 2850 cm^{-1} corresponding to the aliphatic C–H vibrations are detected, which obviously provides evidence for the presence of CTAB in this sample. There is another very broad peak centered at 3195 cm^{-1} , which can be attributed to the O–H stretching vibrations of the adsorbed water on the surface of the powders. After calcination at $150\text{ }^\circ\text{C}$ for 2 h, the intensity of the peak corresponding to the O–H stretching vibrations greatly decreased, indicating the desorption of adsorbed water. However, the two characteristic IR peaks at 2918 and 2850 cm^{-1} of CTAB still existed. After calcination at $400\text{ }^\circ\text{C}$ for 2 h, the C–H vibration peaks of CTAB have disappeared, indicating the decomposition of CTAB molecules attached to the inorganic framework. Figure 3C shows the SAXRD patterns of the product calcined at different temperatures. After calcination at $100\text{ }^\circ\text{C}$, the mesoporous structure was still preserved. However, the diffraction peak was slightly shifted to a d -spacing of 4.2 nm. The shift in the diffraction peak is presumably due to shrinkage in the pore sizes after the calcination. After calcined at $200\text{ }^\circ\text{C}$ for 2 h, the mesoporous structure became less ordered. As a result, the intensity of the diffraction peak significantly decreased. Calcination at $400\text{ }^\circ\text{C}$ leads to the complete extinction of the broad peak, which indicates the disruption of the framework. It shows that the ordered mesoporous structures cannot be preserved after thermal removal of the CTAB surfactants incorporated in the anatase framework.

The pore size and surface area of the product were characterized by nitrogen adsorption–desorption isotherm measurements. A typical nitrogen adsorption–desorption isotherm of the as-prepared sample measured at 77 K is shown in Figure 4a. The Brunauer–Emmett–Teller (BET) surface area of this sample is calculated to be only $8.0\text{ m}^2/\text{g}$, which is much smaller than the expected value. However, it is not surprising because for this uncalcined sample, the occupation of a large amount of template molecules in the pores can lead to incorrect results. Figure 4b shows the nitrogen adsorption–desorption isotherm of the sample after calcination at $400\text{ }^\circ\text{C}$ for 2 h. After calcined at $400\text{ }^\circ\text{C}$, the CTAB molecules occupying the pores are completely decomposed, and reproducible and

reliable BET results were obtained. The calcined sample has a BET surface area of $281.3\text{ m}^2\text{ g}^{-1}$, with pore volume of $0.26260\text{ cm}^3/\text{g}$ (single point at $P/P_0 = 0.9865$). The average pore diameter is calculated to be 5.1 nm. Although after calcination, the ordered pore structure framework has been disrupted, and the sample still has a relatively high surface area with a small pore-size distribution. However, because of the disruption of the frameworks, the arrangement of the pore channels is all random, leading to the extinction of the diffraction peak in the SAXRD patterns.

The as-prepared mesoporous anatase was also characterized by XPS for evaluation of the surface composition. Figure 5A displays the scan survey XPS spectrum which shows the peaks corresponding to oxygen, titanium, carbon, nitrogen, and bromine, providing further proof for the presence of CTAB in the product. Figure 5B exhibits the high-resolution XPS spectrum for the Ti 2p levels. There are two peaks detected in the Ti 2p region. The main peak located at 458.3 eV is assigned to $\text{Ti } 2p_{3/2}$, and the other one at 464.1 eV is corresponding to the $\text{Ti } 2p_{1/2}$. The position of the $\text{Ti } 2p_{3/2}$ is 0.9 eV less than the literature value for Ti^{4+} of rutile/anatase at 459.2 eV.²⁵ The slight red shift in the $\text{Ti } 2p_{3/2}$ position from bulk anatase to the mesoporous structure indicates a change in microenvironments for titanium. This shift is due to the interaction between the remaining surfactant and TiO_2 .^{19,20b} The results show that Ti^{4+} is the existing form of Ti on the surface of the as-prepared mesoporous anatase. Figure 5C gives the O 1s photoelectron peaks of the as-prepared mesoporous anatase. This peak can be resolved into two components. The peak at 530.57 eV corresponds to the lattice oxygen, and the other peak at 532.05 eV corresponds to the adsorbed oxygen on the sample surface. The adsorbed oxygen on the surface of TiO_2 makes the ionizable H^+ hydroxylation to form $-\text{Ti}(\text{OH})-\text{O}-\text{Ti}(\text{OH})-$, which can help the photogenerated holes h^+ to change into OH^\bullet free radicals.^{13a} The OH^\bullet can oxidize most of the organic and part of the inorganic pollutant and degrade them into innocuous substances, such as H_2O and CO_2 . The details about the photocatalytic performance of the as-prepared mesoporous anatase catalyst will be mentioned in the later part of this paper.

In the present study, mesoporous spherical aggregates of anatase nanocrystals are fabricated in a cyclohexane–CTAB–water microemulsion. This strategy is based on the controlled hydrolysis of titanium(IV) sulfate in acidic aqueous media. CTAB is a cationic surfactant, which acts as the structure-directing agent. The interaction between CTAB and the titanium precursor initiates the formation of rodlike micelles. Similar ideas have been proposed by Do Trong On¹⁷ who used cetyltrimethylammonium chloride ($\text{C}_{16}\text{TMA}^+\text{Cl}^-$) as the structure-directing agent and soluble peroxytitanate as a titanium precursor to prepare lamellar and hexagonal mesostructured titania under hydrothermal conditions. The hydrolysis, the condensation of the titanium precursor, and the growth of the in situ generated nuclei were then restricted inside the frameworks of these micelles. The forced hydrolysis of $\text{Ti}(\text{SO}_4)_2$ in acidic aqueous medium can be described as follows:²⁶



(25) Murato, M.; Wakino, K.; Ikeda, S. *J. Electron Spectrosc. Relat. Phenom.* **1975**, *6*, 459.

(26) Wu, R. T.; Wei, Y.; Zhang, Y. F. *Mater. Res. Bull.* **1999**, *34*, 2131.

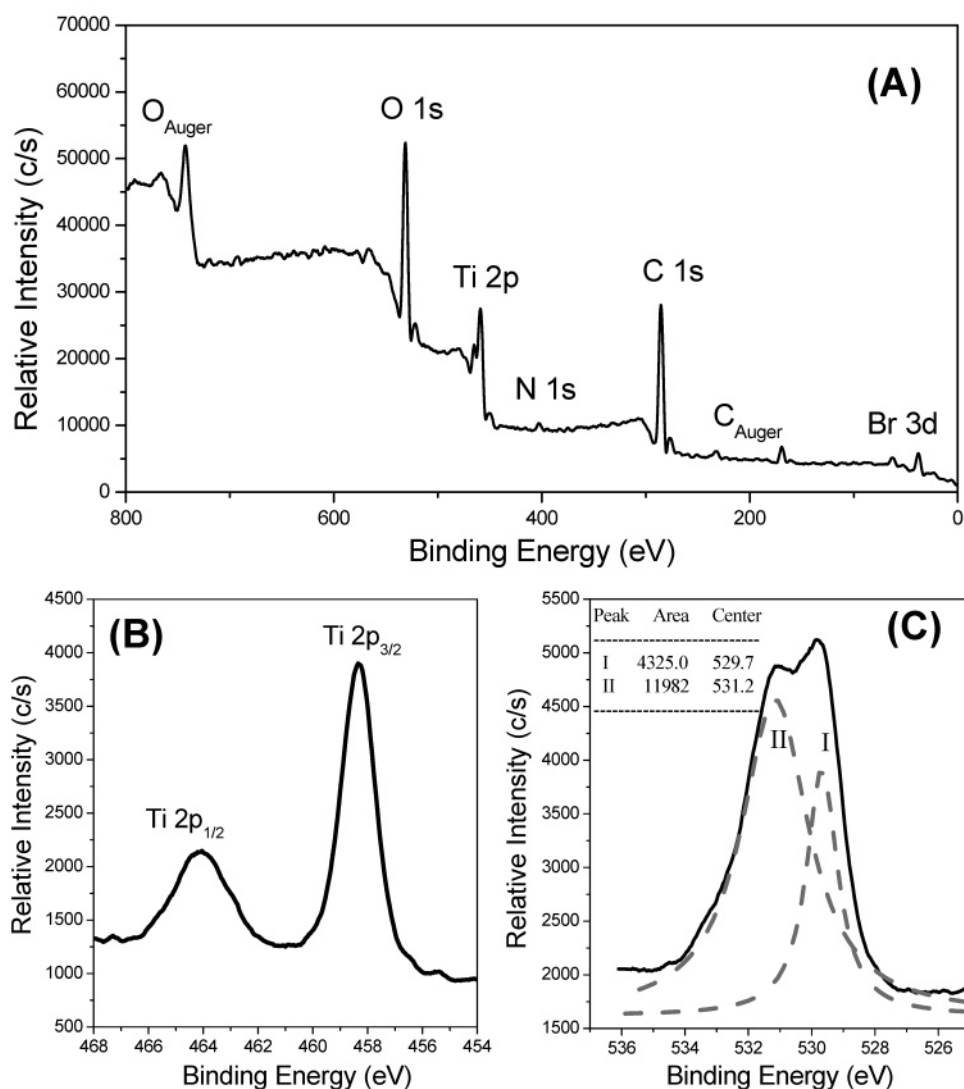


Figure 5. (A) X-ray photoelectron spectroscopic scan survey of the as-prepared mesoporous aggregates of anatase nanocrystals. The peaks have been calibrated with reference to C 1s at 284.6 eV. (B) High-resolution scan of the Ti 2p_{3/2} region. (C) High-resolution scan of the O 1s region.

First, Ti^{4+} hydrolyzed to form $\text{Ti}(\text{OH})_4$, which further condenses into primary clusters that were composed of $m\text{TiO}_2$. Some of the clusters aggregate to form the nuclei and the nanocrystals are formed via further growth of these nuclei. Since the whole process of hydrolysis, condensation, aggregation, and crystallization takes place inside the frameworks of the rodlike micelles, short-range-ordered packing of channels with nanocrystalline anatase walls could be formed. Meanwhile, in the cyclohexane-CTAB-water microemulsion, the amphiphilic CTAB molecules have the tendency to accumulate at the interface between the water phase and the cyclohexane microdroplets, leading to the formation of spherical assemblies. As the "packed channels" self-assemble on the surface of cyclohexane droplets, spherical aggregates of nanocrystalline particles with high textural mesoporosity would be formed finally. The structures, dimensions, and morphologies of the products are affected by both the concentration of CTAB and the volume ratio of cyclohexane: H_2O . Figure 6A shows the SAXRD patterns of the titania powders prepared in the presence of different amounts of CTAB and cyclohexane. When the volume ratio of cyclohexane: H_2O is kept at 1:40 and the concentration of CTAB is in the range of 10.0–30.0 g/L, the position of

the diffraction peak is shifted to higher 2θ values with the decrease in CTAB concentration. When the CTAB concentration is decreased to 10.0 g/L, the position of the diffraction peak is shifted to 2θ at 2.26° , corresponding to a d -spacing value of 3.90 nm. The TEM image of this sample is shown in Figure 6B. It is also noticed that if the CTAB concentration reaches 30.0 g/L, only a broad shoulder is observed, indicating the disordered packing of the pore channels. In the TEM image of this sample (Figure 6C), no ordered pores are observed, which verifies the SAXRD conclusions. When CTAB concentration is kept constant at 20.0 g/L, the position of the diffraction peak did not shift when the cyclohexane: H_2O ratio changed. However, their intensity decreased a little bit with the increase in the cyclohexane: H_2O ratio, indicating the formation of less ordered mesoporous structures. Figure 6D shows a TEM image of the sample prepared in the presence of cyclohexane: H_2O = 3:40 and [CTAB] = 20.0 g/L. This sample is composed of irregular aggregates of nanocrystals with wormhole-like porous structures.

Optical Properties. The study of the optical properties of the materials provides a convenient and effective method for explaining some important features concerning the band structures. To investigate these properties, optical

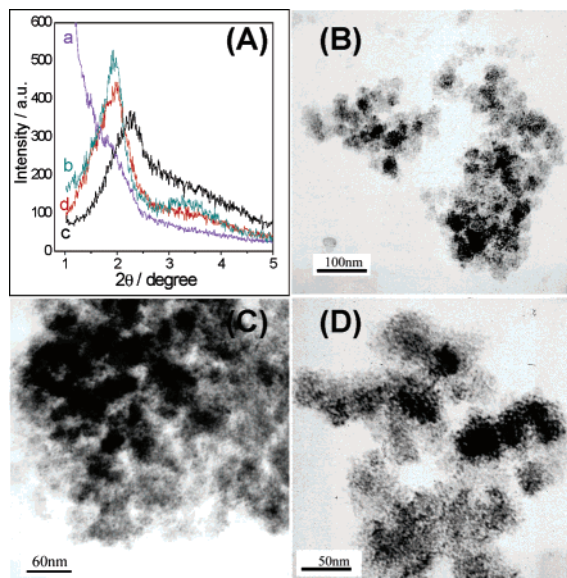


Figure 6. (A) Small-angle powder XRD patterns of anatase powders prepared in the presence of different volume ratio of cyclohexane:H₂O and CTAB concentrations: (a) cyclohexane:H₂O = 1:40 and [CTAB] = 30.0 g/L, (b) cyclohexane:H₂O = 1:20 and [CTAB] = 20.0 g/L, (c) cyclohexane:H₂O = 1:40 and [CTAB] = 10.0 g/L, (d) cyclohexane:H₂O = 3:40 and [CTAB] = 20.0 g/L. (B) TEM image of the anatase powders prepared in the presence of cyclohexane:H₂O = 1:40 and [CTAB] = 10.0 g/L. (C) TEM image of the anatase powders prepared in the presence of cyclohexane:H₂O = 1:40 and [CTAB] = 30.0 g/L. (D) TEM image of the anatase powders prepared in the presence of cyclohexane:H₂O = 3:40 and [CTAB] = 20.0 g/L.

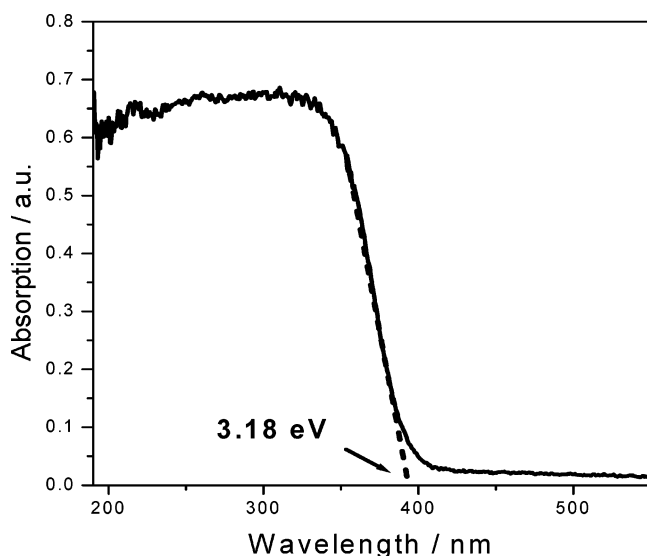


Figure 7. Diffuse reflection spectrum of the as-prepared mesoporous aggregate of anatase nanocrystals at room temperature.

transmission or reflection spectra are most commonly measured. Since our product is in the form of powders, we employed diffuse reflection spectroscopy measurements as the characterization tool. The diffuse reflection spectrum of the as-prepared mesoporous anatase measured at room temperature is shown in Figure 7. The optical absorption threshold is located approximately at 391 nm which corresponds to a band gap energy of 3.18 eV. This value is very close to the band gap energy of anatase bulk material ($E_g = 3.2$ eV). The electronic band structure of titania was reported by Daude and co-workers.²⁷ Titania crystals, both rutile and anatase, have a tetragonal unit

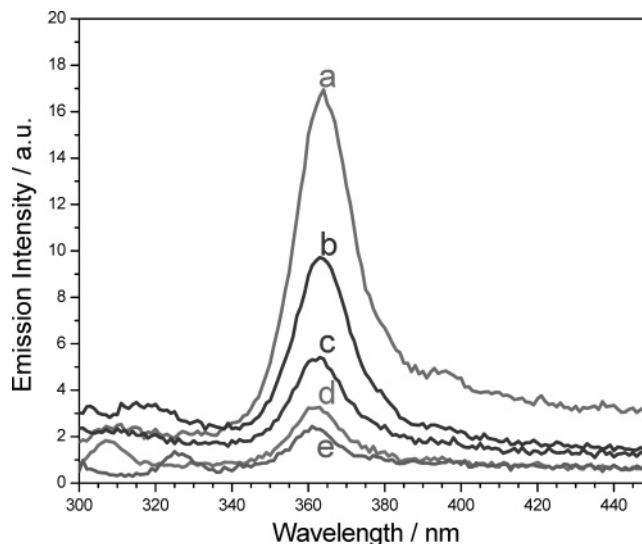


Figure 8. Photoluminescent emission of the as-prepared mesoporous aggregate of anatase nanocrystals at room temperature with excitation wavelength of (a) 235 nm, (b) 250 nm, (c) 265 nm, (d) 275 nm, and (e) 290 nm.

cell and possess highly ionic lattice.²⁸ Therefore, the valence band is mainly composed of the outermost p electrons of oxygen and the corresponding wave functions are considerably localized on O²⁻ lattice sites. The lowest conduction band would be chiefly composed of the excited states of Ti⁴⁺. The onset of absorption at 3.18 eV corresponds to the band gap energy of anatase and is ascribed to the indirect transition, $\Gamma_3 \rightarrow X_{1b}$, which was predicted theoretically to occur at 3.19 eV.²⁹

Another unique property associated with semiconductor nanocrystals is their luminescence characteristics, with specific emission wavelengths dependent upon the band structures of semiconductors and physical dimensions, as well as the chemical environments. Here, we use ultraviolet excitation source (λ in the range of 220–300 nm) to induce the luminescence of the as-prepared mesoporous anatase at room temperature. Figure 8 shows the photoluminescent emission spectra of the mesoporous anatase with different excitation wavelengths. The emission differs in intensity with the change in the excitation wavelength, while the maximum position remains constant, centered at 362 nm (3.45 eV). The intensity of this emission peak decreased with the increase in excitation wavelength from 235 to 290 nm. This emission corresponds to the degenerated direct transition $X_{1b} \rightarrow X_{2b}/X_{1a}$.²⁹ There are other two weak emissions detected. One is centered at 308 nm (4.02 eV) when the excitation wavelength is 275 nm, which can be assigned to the direct transition, $\Gamma_{1b} \rightarrow \Gamma_{5b}$.²⁹ The other is located at 327 nm (3.80 eV) when the excitation wavelength is 290 nm, corresponding to the direct transition $\Gamma_2 \rightarrow \Gamma_{1b}$.²⁹ Electronic transitions in semiconductors must conserve momentum, and photon momentum is very low. Indirect transitions, therefore, implicate simultaneous interactions between photons and lattice phonons.³⁰ As a result, emission probabilities of indirect transitions are much lower than those of direct transitions. Therefore, in the emission spectral range surveyed in our study (300–500 nm), no emission corresponding to indirect transitions is detected.

(27) Daude, N.; Gout, C.; Jouanin, C. *Phys. Rev. B* **1977**, *15*, 3229.

(28) Kahn, A. H.; Leyendecker, A. *J. Phys. Rev.* **1964**, *135*, A1321.

(29) Serpone, N.; Lawless, D.; Khairutdinov, R. *J. Phys. Chem.* **1995**, *99*, 16646.

(30) Mooser, E.; Oearson, W. B. In *Progress in Semiconductors*; Gibson, A. F., Ed.; John Wiley & Sons: New York, 1960; Vol. 3, p 53.

Photocatalytic Performance. The presence of several organic pollutants in industrial wastewater results in a series of environmental problems. Photocatalytic oxidation using semiconductors as the catalysts is one of the advanced oxidation processes for the rapid and convenient removal of such organic pollutants. Although several semiconductors such as CdS, ZnO, and WO_3 have been used, titania has been the most popular photocatalysts in photocatalytic oxidation for wastewater treatment because of its nontoxicity, chemical inertness, photostability, and low costs.¹³ In the past few years, a wide variety of novel titania photocatalysts have been fabricated and their photocatalytic performance has been studied intensively.³¹ Generally speaking, the photocatalytic activity of amorphous titania is negligible, and the rutile form of titania is less photoactive than anatase.^{13c,32} To get high photocatalytic activity, anatase powders with high crystallinity and high surface area are usually used as the photocatalysts. The as-prepared mesoporous spherical aggregates of anatase nanocrystals meet the above-mentioned criteria. In addition, the wormhole channel motif is a potentially important structural feature for catalytic activity, because channel branching within the framework provides easy access to the reactive sites on the framework wall. Therefore, it can be regarded as an ideal candidate for high photocatalytic activity. In the present study, the as-prepared mesoporous anatase powders have been used to catalyze the photoinduced degradation of various types of organic dye pollutants, including methyl orange, bromopyrogallol red, and methylene blue.

Figure 9 shows the UV-vis absorption spectra of methyl orange aqueous solution recorded at different time intervals during the mesoporous anatase catalyzed photodegradation. The initial concentration of methyl orange is 30.0 mg/L, and the loading of mesoporous anatase catalyst is 3.0 g/L. The absorption peak centered at 426 nm is the characteristic peak of methyl orange, and the absorption at 426 nm follows the Beer-Lambert law in the concentration range from 0 to 50.0 mg/L. The intensity of the absorption peak kept decreasing as the reaction time increased. After 45 min, this peak completely disappeared, indicating the complete degradation of methyl orange in the solution. By measuring the peak areas, we can get the plots of methyl orange concentration versus reaction time.

The ordered mesoporous structure of the as-prepared anatase catalyst was of key importance to the high photocatalytic activity. As illustrated in Figure 10, with the increase in the calcination temperature, the porous structure became less ordered; as a result, the photocatalytic activity of the catalyst significantly decreased. For a nonporous anatase catalyst (commercial anatase

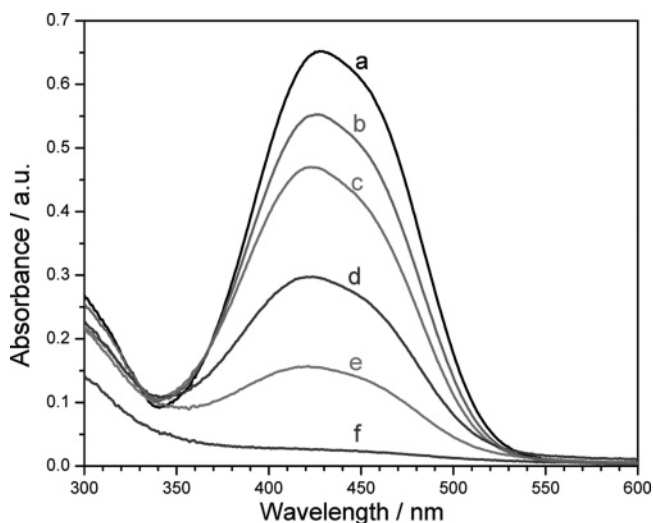


Figure 9. UV-vis absorption spectra of methyl orange aqueous solution recorded at different time intervals following mesoporous anatase catalyzed photodegradation. The spectra were recorded at time intervals of (a) 0 min, (b) 5 min, (c) 10 min, (d) 20 min, (e) 30 min, (f) 45 min. The initial concentration of methyl orange is 30.0 mg/L, the loading of mesoporous anatase catalyst is 3.0 g/L.

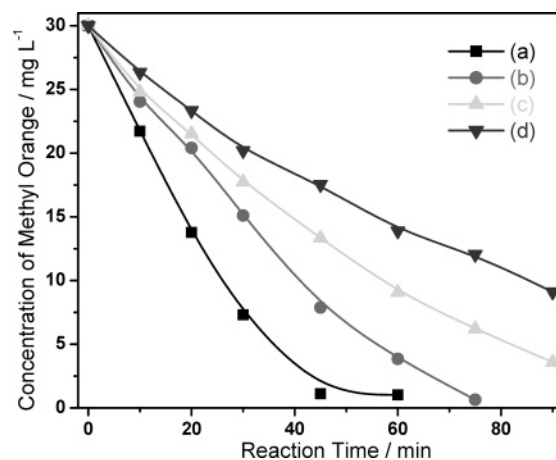


Figure 10. Plots of the concentrations of methyl orange vs reaction time by using different anatase powder samples as the catalyst: (a) the as-prepared mesoporous anatase, (b) after calcinations at 200 °C for 2 h, (c) after calcinations at 400 °C for 2 h, and (d) commercial anatase nanoparticles with an average diameter of 30 nm and BET surface area of 80 m² g⁻¹. The loadings of catalyst are all 3.0 g/L. The initial concentration of methyl orange is 30.0 mg/L.

nanoparticles with an average diameter of 30 nm and BET surface area of 80 m² g⁻¹), the photocatalytic activity is much lower, even though both the nonporous anatase nanoparticles and the mesoporous aggregates have comparable average particle diameters.

The effects of catalyst loading on the photocatalytic degradation of methyl orange were studied by varying the amount of mesoporous anatase from 0 to 4.0 g/L. Figure 11A describes the photocatalytic degradation of 30.0 mg/L methyl orange in aqueous anatase dispersion with different catalyst loadings. It can be seen that in the absence of mesoporous anatase catalyst, there is almost no detectable degradation. Increasing the loading of anatase catalyst from 1.0 to 3.0 g/L can greatly accelerate the degradation. With the augmentation of anatase, the probability of absorbing photons increases. This can lead to the large generation of OH^\cdot free radicals, and the photocatalytic degradation rate will increase greatly.

(31) For some recent examples, see (a) Du, Y.; Rabani, J. *J. Phys. Chem. B* **2003**, *107*, 11970. (b) Li, X. Z.; Liu, H.; Cheng, L. F.; Tong, H. *J. Environ. Sci. Technol.* **2003**, *37*, 3989. (c) Sivalingam, G.; Nagaveni, K.; Hegde, M. S.; Madras, G. *Appl. Catal., B* **2003**, *45*, 23. (d) Cozzoli, P. D.; Comparelli, R.; Fanizza, E.; Curri, M. L.; Agostiano, A. *Mater. Sci. Eng., C* **2003**, *23*, 707. (e) Malinowska, B.; Walendziewski, J.; Robert, D.; Weber, J. V.; Stolarski, M. *Appl. Catal., B* **2003**, *46*, 441. (f) Guillard, C.; Disdier, J.; Monnet, C.; Dussaud, J.; Malato, S.; Blanco, J.; Maldonado, M. I.; Herrmann, J. M. *Appl. Catal., B* **2003**, *46*, 319. (g) Arabatzis, I. M.; Stergiopoulos, T.; Andreeva, D.; Kitova, S.; Neophytides, S. G.; Falaras, P. *J. Catal.* **2003**, *220*, 127. (h) Mills, A.; Hill, G.; Bhopal, S.; Parkin, I. P.; O'Neill, S. A. *J. Photochem. Photobiol., A* **2003**, *160*, 185. (i) Ren, T. Z.; Yuan, Z. Y.; Su, B. L. *Chem. Phys. Lett.* **2003**, *374*, 170. (j) Hurum, D. C.; Agrios, A. G.; Gray, K. A.; Rajh, T.; Thurnauer, M. C. *J. Phys. Chem. B* **2003**, *107*, 4545. (k) Mills, A.; Elliott, N.; Parkin, I. P.; O'Neill, S. A.; Clark, R. J. *J. Photochem. Photobiol., A* **2002**, *151*, 171. (l) Vamathevan, V.; Amal, R.; Beydoun, D.; Low, G.; McEvoy, S. *J. Photochem. Photobiol., A* **2002**, *148*, 233. (m) Ruan, S.; Wu, F.; Zhang, T.; Gao, W.; Xu, B.; Zhao, M. *Mater. Chem. Phys.* **2001**, *69*, 7.

(32) Brown, J. D.; Williamson, D. L.; Nozik, A. J. *J. Phys. Chem.* **1985**, *89*, 3076.

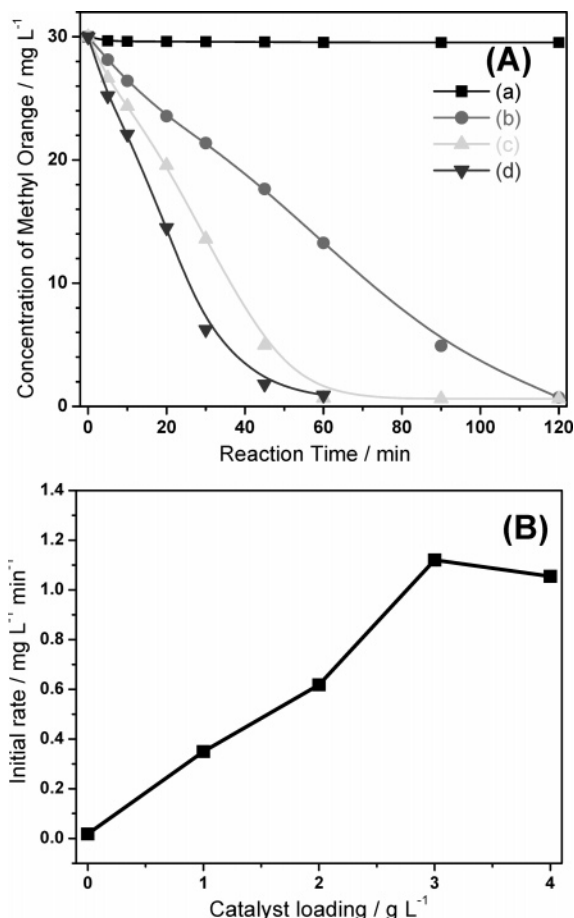


Figure 11. (A) Effect of the loading of mesoporous anatase catalyst on photodegradation of methyl orange. The figure shows the concentrations of methyl orange at different time intervals. The loadings of catalyst are (a) 0, (b) 1.0 g/L, (c) 2.0 g/L, and (d) 4.0 g/L mesoporous anatase. The initial concentration of methyl orange is 30.0 mg/L. (B) The variation of initial rate with catalyst loading. The initial concentration of methyl orange is 30.0 mg/L.

However, further increasing the loading from 3.0 to 4.0 g/L did not lead to conspicuous increase in the degradation rate. We have tried to calculate the initial degradation rate according to the modified Langmuir–Hinshelwood (L–H) model.³³ The variation of initial rate with catalyst loading is shown in Figure 11B. The initial rates reaches saturation for catalyst loading above 3.0 g/L, suggesting that the substrate molecules are not sufficient for adsorption by the increased amount of anatase catalyst above this concentration. In addition, when the loading of catalyst is higher than a critical concentration, the depth of penetration of light in the reactor cannot increase anymore, while scattering of light and collision of anatase catalyst is increased, and thus a negative effect on the reaction rate develops. Therefore, the degradation rate of methyl orange increases with the amount of catalyst only till a specific limit is reached.

The effect of initial concentration of methyl orange on the photocatalytic degradation rate has also been investigated over the concentration range of 10.0–40.0 mg/L, since the pollutant concentration is an important parameter in water treatment. Experimental results are presented in Figure 12A. The initial concentration has a significant effect on the degradation rates. As illustrated in Figure 12B, the initial rate increases with the increase

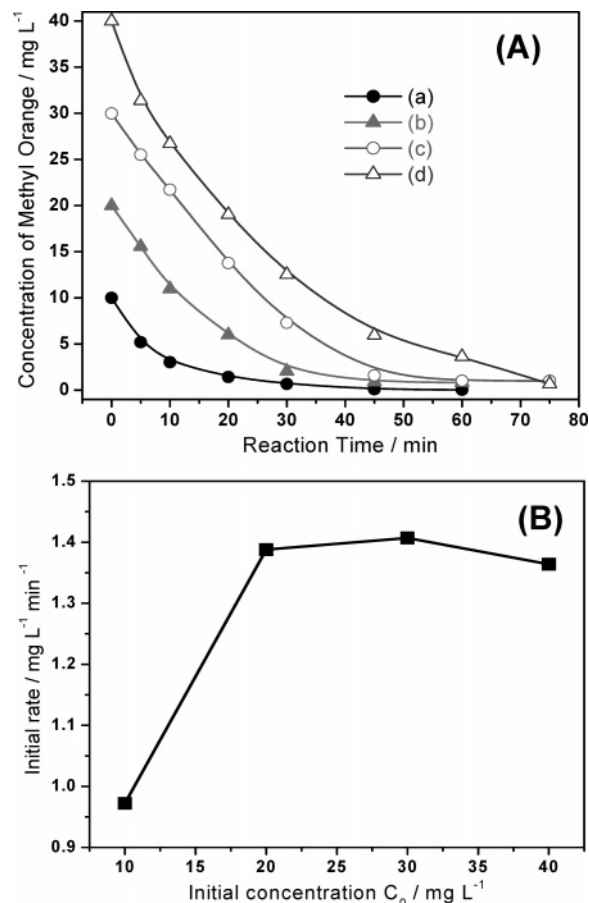


Figure 12. (A) Effect of the initial concentration of methyl orange on the photodegradation. The figure shows the concentrations of methyl orange at different time intervals. The initial concentrations of methyl orange are (a) 10.0 mg/L, (b) 20.0 mg/L, (c) 30.0 mg/L, (d) 40.0 mg/L. The catalyst loading is 3.0 g/L. (B) The variation of initial rate with catalyst loading. The catalyst loading is 3.0 g/L.

in initial concentrations at low concentrations (below 20.0 mg/L) and saturates at higher concentrations.

The as-prepared mesoporous anatase catalyst can also be effectively used to catalyze the photodegradation of some other organic dyes, such as bromopyrogallol red and methylene blue (see Supporting Information). By using this catalyst, the complete degradation of bromopyrogallol red with an initial concentration of 20.0 mg/L could be accomplished in only about 30 min when the catalyst loading was 1.0 g/L. For methylene blue, the as-prepared anatase powders also exhibit a high photocatalytic activity. The 8.0 mg/L methylene blue almost completely degraded in about 90 min when the catalyst loading was 3.0 g/L.

IV. Conclusions

In summary, a facile and efficient approach for the fabrication of mesoporous spherical aggregates of anatase nanocrystals has been established. Cationic surfactant CTAB was used as the structure-directing agent, and the interaction between cyclohexane microdroplets and the CTAB self-assemblies leads to the assembly of 4–5-nm-sized anatase nanocrystals into spherical aggregates with wormhole-like mesoporous structures. The structures, morphologies, compositions, and optical properties of the product have been characterized. The as-prepared mesoporous anatase exhibits high photocatalytic activity and can be effectively used as the catalyst for the room-temperature photodegradation of a variety of organic dye

(33) Al-Ekabi, H.; Serpone, N. *J. Phys. Chem.* **1988**, *92*, 5726.

pollutants including methyl orange, bromopyrogallol red, and methylene blue. Upscaling of this approach will lead to large-scale production of mesoporous anatase photocatalyst with high catalytic activity and efficiency, which have wide applications in the treatment of environmental pollutants. We are now trying to design optimized photoreactors which can further increase the photocatalytic efficiency and make the catalyst reusable.

Supporting Information Available: Calculation of the initial degradation rates based on the modified Langmuir–Hinshelwood (L-H) model and photoinduced degradation of

methylene blue and bromopyrogallol red catalyzed by mesoporous anatase. This material is available free of charge via the Internet at <http://pubs.acs.org>.

Acknowledgment. This work is supported by the National Natural Science Foundation of China under project numbers 20325516 and 90206037. The work is also supported by Science and Technology Foundation of Jiangsu, China under project number BK 2004210.

LA0477892